# Spectroscopic Survey of Red Giants in the SMC. I: Kinematics [1]

Jason Harris & Dennis Zaritsky

*Steward Observatory*

*933 North Cherry Ave., Tucson, AZ, 85721*

jharris@as.arizona.edu, dzaritsky@as.arizona.edu

## ABSTRACT

We present a spectroscopic survey of 2046 red giant stars, distributed over the central 4 kpc×2 kpc of the Small Magellanic Cloud (SMC). After fitting and removing a small velocity gradient across the SMC (7.9 km s$^{-1}$ deg$^{-1}$ oriented at 10° E of N), we measure an rms velocity scatter of $27.5 \pm 0.5$ km s$^{-1}$. The line of sight velocity distribution is well-characterized by a Gaussian and the velocity dispersion profile is nearly constant as a function of radius. We find no kinematic evidence of tidal disturbances. Without a high-precision measurement of the SMC's proper motion, it is not possible to constrain the SMC's true rotation speed from our measured radial-velocity gradient. However, even with conservative assumptions, we find that $v < \sigma$ and hence that the SMC is primarily supported by its velocity dispersion. We find that the shape of the SMC, as measured from the analysis of the spatial distribution of its red giant stars, is consistent with the degree of rotational flattening expected for the range of allowed $v/\sigma$ values. As such, the properties of the SMC are consistent with similar low luminosity spheroidal systems. We conclude that the SMC is primarily a low luminosity spheroid whose irregular visual appearance is dominated by recent star formation. A simple virial analysis using the measured kinematics implies an enclosed mass within 1.6 kpc of between 1.4 and $1.9 \times 10^9 M_\odot$, and a less well constrained mass within 3 kpc of between 2.7 and $5.1 \times 10^9 M_\odot$.

*Subject headings:* galaxies: evolution — galaxies: stellar content — galaxies: Magellanic Clouds — galaxies: individual: Small Magellanic Cloud

---

[1]This paper includes data gathered with the 6.5 meter Magellan Telescopes located at Las Campanas Observatory, Chile.

## 1. Introduction

There is an abundant and growing body of evidence that gravitational interactions have been critical in the evolution of the Magellanic Clouds. One prominent piece of evidence is the existence of the Magellanic Stream (Mathewson et al. 1974), a roughly contiguous filament of neutral hydrogen that stretches more than 150 kpc behind the Clouds and which numerical simulations suggest was stripped by a recent interaction among the Clouds and the Milky Way (Gardiner & Noguchi 1996). The Clouds are the nearest galaxies that are globally affected by interactions yet are far from being disrupted. As such, they are detailed examples of galaxies expected to be common in a hierarchical model of structure formation and may provide general insights on how such weak interactions affect both the observed characteristics and evolution of galaxies.

For the Small Magellanic Cloud (SMC), we have presented results on the effects of the interactions on both its global properties and its evolution. First, we demonstrated that the irregular appearance of the SMC is due solely to recent star formation, because its older stellar populations are distributed in a regular, smooth ellipsoid (Zaritsky et al. 2000). This result cautions us that galaxies that appear to be irregular, particularly low mass galaxies like the SMC, may indeed have quite a different underlying structure — a conclusion that is obviously critical to such considerations as whether dIrr's can evolve into dE's. Second, we found that the SMC has experienced periodic episodes of global enhanced star formation, suggesting triggering by perigalactic passes with the Large Magellanic Cloud and with the Milky Way (Harris & Zaritsky 2004; Zaritsky & Harris 2004). These results demonstrate for one galaxy, and suggest for others, that basic observational parameters such as morphology, luminosity, and color are significantly affected by star formation induced by weak interactions. Here, we investigate (1) whether such interactions also induce detectable kinematic disturbances, and so whether common kinematical analyses, such as the classification of galaxies by the ratio of rotational velocity to velocity dispersion and the application of the virial theorem to estimate the mass, are valid for galaxies affected by weak interactions and (2) whether the classification of the SMC as a dE based on the distribution of the older stars (Zaritsky et al. 2000) is substantiated by the kinematics.

The conventional picture of the SMC as a disturbed galaxy is derived from the kinematics of stars in its outer regions (Hatzidimitriou et al. 1993, 1997), and from a large observed line-of-sight depth (Hatzidimitriou & Hawkins 1989; Gardiner & Hawkins 1991; Crowl et al. 2001). It is important to note that these line-of-sight depth studies also generally sample the outer regions of the SMC. The depth of the central regions of the SMC has been probed using Cepheid variables, but there seems to be no consensus on the resulting depth. While some authors find a large line-of-sight depth of around 20 kpc (Mathewson et al. 1986, 1988;

Groenewegen 2000), others conclude the depth is only 6–8 kpc (Welch et al. 1987; Lah et al. 2005). Much of the controversy can be resolved by simply recognizing that the term "depth" is used differently by the two groups of authors. Those who define the depth as the full front-to-back extent of the tracer population obtain a depth around 20 kpc, while those who define the depth as the full width at half-maximum of the distribution of distances obtain a much smaller depth around 6–8 kpc. The conclusion to be drawn from this body of work is that while the outer regions of the SMC may be extended along the line of sight (up to 20 kpc), especially toward the Northeast, its central region seems to be only modestly extended, with a depth of 6–8 kpc.

Our knowledge of the internal kinematics of the main body of the SMC, the region that would typically be observed in more distant galaxies, is surprisingly limited, considering the SMC's proximity and suspected complex internal structure. Previous studies have determined mean radial velocities and velocity dispersions, based on modest numbers of tracer populations: 44 central planetary nebulae (Dopita et al. 1985), 12 outer RGB stars (Suntzeff et al. 1986), 131 central Carbon stars (Hardy et al. 1989), 30 outer red clump stars (Hatzidimitriou et al. 1993), and 70 outer Carbon stars (Hatzidimitriou et al. 1997). In each case, the observed sample was too small to support analysis beyond the mean velocity and velocity dispersion of the sample.

In this paper, we present a spectroscopic survey of over 2000 red giant branch stars in the main body of the SMC, using the Inamori Magellan Areal Camera and Spectrograph (IMACS; Bigelow et al. 1998) at the Magellan Baade Telescope at Las Campanas Observatory in Chile. In Section 2, we describe the observations and data reduction. In Section 3, we discuss whether the SMC kinematics follow the expectations for a dE and whether we find any kinematic signature of the weak interactions the SMC has recently experienced. We summarize the results in Section 4.

In addition to obtaining radial-velocity kinematics of a large sample of SMC field stars, the observations were also designed to yield metallicities based on the equivalent width of the Ca II triplet feature. The metallicities of our sample and their constraint on the chemical enrichment history of the SMC are presented in a subsequent paper (Harris 2005).

## 2. Observations and Data Reduction

### 2.1. Sample Selection

We select candidate red giant branch (RGB) stars photometrically from our Magellanic Clouds Photometric Survey (MCPS) catalog, which contains subarcsecond astrometry and

$UBVI$ photometry for over 6 million SMC stars (Zaritsky et al. 2002). We employ the following photometric criteria to select candidate RGB stars:

$$15.4 < I < 16.4$$

and

$$(20.50 - 4.0 \times (V - I)) < I < (22.0 - 4.0 \times (V - I))$$

These photometric criteria are plotted on a $V - I, I$ Hess diagram of the SMC in Figure 1. The bright limit ($I > 15.4$ mag) excludes stars near the tip of the RGB, where deep mixing may alter the surface abundances. The faint limit ($I < 16.4$ mag) ensures that we can obtain spectra with S/N$\gtrsim$ 20 in a 40-minute exposure. The diagonal cuts were designed to be roughly parallel to the fiducial RGB of the SMC stellar population. Approximately 34,000 candidate RGB stars throughout the $4.5° \times 4°$ region covered by the MCPS satisfy these criteria.

In addition to RGB stars, we also select a sample of alignment stars for precision positioning of the slitmasks. A key consideration for slitmask alignment is that the alignment stars are drawn from the same catalog as our target stars and hence share the same astrometric system. Because our SMC fields are much more crowded than a typical pointing on the sky, we restrict our alignment-star selection to a narrow range of brightnesses ($17.0 < I < 17.5$), at the bright end of the range of magnitudes recommended in the IMACS user manual. We also impose a color cut ($0.5 < (V - I) < 1.5$), to further reduce the large number of candidates. Lastly, we reject crowded objects, those that are less than $20''$ from neighboring stars brighter than $I = 17.5$ mag. We are left with approximately 13000 uncrowded alignment star candidates throughout the SMC.

We use these photometrically-selected RGB and alignment star samples as input for the IMACS slitmask design program `intgui`. Our sixteen selected fields cover the central 3.9 kpc×1.8 kpc of the SMC (see Figure 2). In each of these fields, we interactively select between 7 and 12 alignment stars from the dozens available to uniformly cover the field of view. The slit design package optimally selects objects from the candidate target list to fill the detector plane with non-overlapping spectral traces. It employs an internal model of the optical geometry of IMACS to predict the spectral trace of each potential target in a given field on the detector plane. A target is only selected for observation if its predicted spectral trace on the detector includes a predefined wavelength interval of interest. Because we are targeting the Ca II triplet, we selected a wavelength interval from 8000 Å to 9000 Å. After determining the set of objects whose spectra fall on the detector properly, `intgui` determines whether there are overlapping traces, and eliminates objects until no overlaps remain. One can assign weights to candidate objects to modulate the likelihood that they are selected for

observation, but we chose the default uniform weighting. We chose a short slit length (4″), to maximize the number of slits per mask. Our final masks contain an average of 270 slits (ranging from 122 to 359), which is roughly half of the available RGB candidates in each field. Table 1 presents the following data for each prepared field: (1) the field identification number; (2) the Right Ascension coordinate of the field center; (3) the Declination coordinate of the field center; and (4) the number of slits placed on RGB candidates in the field. The remaining columns of Table 1 are described in Section 2.5.

## 2.2. Observations

We observed 14 of our 16 fields over four half-nights on the Magellan Baade telescope, from August 29 to September 1, 2004. Each night was clear, with seeing between 1″ and 1.5″. Our fields were observed at an airmass between 1.4 and 1.5, and the moon was nearly full throughout the run. We used the f/2 camera, which images a 27.4′ diameter field onto the 8k×8k CCD detector array, with an image scale of 0.2″ per pixel. We used the 600 l mm$^{-1}$ grism blazed at 34°, which covers 5600 Å to 10000 Å in first order, at a resolution of 0.583 Å per pixel. Our slits are 1″ wide, so the effective spectral resolution is 2.9 Å per resolution element. We used the Clear filter to obtain the widest possible wavelength coverage.

An iterative procedure is required to obtain precision pointing that ensures that each slit is correctly illuminated by the corresponding target object. After pointing the telescope to the field center coordinates, we obtain a short direct-image exposure of the mask. We measure the positional offsets of the 7–12 alignment stars in the field with respect to the centers of their square alignment holes in the mask. We then adjust the telescope pointing and field rotation angle to correct for these offsets, and take another direct image of the mask. The process is repeated until the alignment star offsets are minimized (this typically requires only two iterations). There were two fields (01 and 06) for which we could not simultaneously center all alignment stars. We performed the best alignment that we could following the described procedure, but determined later that these fields still suffered from non-negligible pointing and field-rotation errors (see Section 2.5).

The remaining observational details are straightforward. With the 600 l mm$^{-1}$ grism, IMACS has a total throughput efficiency of about 6% at 8500 Å. For the first field observed (field 04), we obtained three exposures of 1200 s. However, from those images we determined that two 1200 s exposures would be sufficient to obtain S/N = 25 to 50 for our $I \simeq 16$ mag targets. The remaining fields were observed with $2 \times 1200$ s exposures. Each observation was immediately followed by a pair of flat-field exposures obtained without changing the telescope orientation by moving an illuminated flat-field screen into the optical path. We

obtained arc-lamp exposures of each field in the daytime, which is sufficient for a first-order wavelength solution. We use the night-sky lines embedded in the target spectra for our final wavelength calibration (see Section 2.3). A series of ten bias exposures was also obtained each afternoon.

## 2.3. Data Reduction

We use IRAF[1] and the COSMOS reduction package, the latter of which is designed specifically to reduce, calibrate, and extract multislit IMACS spectra. COSMOS consists of a collection of programs, each of which performs a specific data-reduction task with minimal input required from the user. In the following description of our procedure, we designate IRAF tasks as I:`task` and COSMOS tasks as C:`task`.

We use I:`zerocombine` to combine our ten daily bias exposures into a master bias image for each night. We then run C:`Sflats`, which removes the bias from the flat field images, combines multiple exposures to reject cosmic rays, and normalizes each combined flat to a mean pixel value of 1.0. To complete the preliminary image processing, we run C:`biasflat` on each spectroscopic image to subtract the bias and divide by the corresponding normalized flat-field image.

We used a two-step process to simultaneously fit a 2-D spectral trace to each slit, and determine a preliminary wavelength calibration. We first ran C:`align-mask`, which uses an internal model of the optical geometry of IMACS and the known positions of each slit in a given mask to predict the spectral trace of each spectrum on the detector plane. The predicted traces are then refined by matching to the arc-lamp spectral images, using the C:`map-spectra` task. C:`map-spectra` uses third-order polynomials to fit the tilt, curvature and width of each trace, and it uses the known emission-line features in the arc lamp spectra to simultaneously fit a fifth-order polynomial along the dispersion direction of each trace.

The standard COSMOS procedure is to run C:`subsky` *before* extracting the spectra, which produces better results since the sky pixels are not resampled. However, we postpone sky subtraction because we will use the sky emission lines for our final wavelength calibration. Therefore, we next use C:`extract-2dspec` to apply the optimized trace models to the data images, and extract the rectified, wavelength-calibrated, two-dimensional spectra from each

---

[1]IRAF is the Image Reduction and Analysis Facility, distributed by the National Optical Astronomy Observatories, which are operated by the Association of Universities for Research in Astronomy, Inc., under cooperative agreement with the National Science Foundation.

individual field exposure. We use C:sumspec to combine each extracted exposure pair and reject cosmic rays (C:sumspec adopts the average pixel value of the pair, unless the two pixel values differ by more than $3\sigma$, in which case it adopts the lower value).

The density of emission lines in the observed spectral region (7000 Å$< \lambda < 10000$ Å) is more than sufficient to support a robust wavelength calibration. We define and apply the wavelength calibration using the standard IRAF pipeline of I:identify, I:reidentify, I:fitcoords, and I:transform. I:identify is run on a single representative slit from each field that is selected to cover a wide wavelength range with large S/N. I:identify uses a database of spectral features with known wavelengths to determine the wavelength solution. We choose the "lowskylines" database, which is included with IRAF and is appropriate for night sky lines in a low-resolution spectrum. Because the spectra already have a first-order calibration from the COSMOS fit to our daily emission lamp spectra, we do not need to manually identify any spectral features and instead we allow I:identify to automatically identify emission features from the "lowskylines" database. We fit a fourth-order Chebyshev function to minimize the deviations of the observed line centers from their known positions and obtain a refined wavelength solution. We reject points which deviate from the wavelength solution by $> 3\sigma$ as outliers and recompute the fit. We then reidentify features using the improved model and iterate the fit until we reach a solution that has an RMS < 0.3 Å.

We run I:reidentify on all remaining slit images in the field, using the wavelength calibration found by I:identify as a starting point, and automatically determining an optimal wavelength solution for each slit. I:reidentify determines an independent wavelength solution for every fourth row in each two-dimensional slit image (for a total of five rows per slit), and uses the same fitting function (fourth order Chebyshev) and set of emission lines as used by I:identify. Next, we run I:fitcoords to fit a two-dimensional surface to the set of five wavelength solutions for each slit obtained by I:reidentify. I:fitcoords uses a second-order Chebyshev function in the dispersion direction and a first-order Chebyshev function in the spatial direction to fit the surface. Finally, we use I:transform and the two-dimensional wavelength solution to rectify each image.

The final reduction step is to extract the one-dimensional spectral trace of each target star from its rectified slit image and subtract the sky using the I:apall task. I:apall works well in its non-interactive mode for these data because most of the curvature in the spectral trace has already been removed by the two-dimensional COSMOS extraction. A sample of the extracted one-dimensional spectra from one of our fields is shown in Figure 3.

To check the quality of the wavelength calibration, we select a subset of prominent sky emission lines and measure their wavelength in the set of 2079 rectified, 1-dimensional extracted spectra for which sky subtraction was omitted (see Figure 4). The standard devia-

tion of the distribution of measured sky line positions is between 0.25 Å and 0.30 Å (roughly 0.1 resolution element). The mean deviation of the measured line positions is 0.09 Å, corresponding to a velocity uncertainty of 3 km s$^{-1}$.

## 2.4. Measuring Line Profiles

We measure the central wavelengths and equivalent widths of the Ca II triplet lines at 8498 Å, 8542 Å and 8663 Å in each of our red giant spectra to determine the stellar radial velocity and calcium-triplet metallicity. Each line is fit independently, with no *a priori* constraint on their relative position or line strength. We isolate 20 Å segments of the spectrum, centered on the expected wavelength of each line (assuming a mean radial velocity for the SMC), and fit a straight-line segment (for the stellar continuum) plus an inverted Gaussian function (for the line profile) to each segment. The fit parameters of the Gaussian yield the central wavelength and equivalent width of each line. To estimate the uncertainty on these quantities, we employ a Monte Carlo technique. We construct 50 realizations of the spectral segments by perturbing each pixel's flux value according to its estimated uncertainty. We fit for the central wavelength and equivalent width in each of these realizations, and adopt the standard deviation of their distribution as the estimated internal uncertainty of our measurements.

The radial velocity of each star is determined using the mean Doppler shift of the three calcium lines relative to their known rest wavelengths. The distribution of uncertainties in the measured doppler shift is very tightly peaked at 0.08 Å, and 97% of the stars have a measurement uncertainty below 0.6 Å. However, there is a long, sparsely-populated tail in the distribution, to uncertainty values as high as 3 Å. Most of the spectra with large uncertainties are polluted by spectral-overlap artifacts that were not flagged in our visual inspection of the sample (see below). We reject objects whose uncertainty in the Doppler shift of the Calcium lines exceeds 0.6 Å, corresponding to a maximum allowed radial velocity error of 20 km s$^{-1}$ (see Figure 5).

Of the 3650 observed slits, we successfully extracted 3416 one-dimensional spectra. Of these, 789 were rejected due to large artifacts in the extracted spectrum, 240 spectra were rejected because fewer than two Calcium lines could be measured, and another 82 spectra were rejected because their estimated radial velocity uncertainty exceeded 20 km s$^{-1}$. This leaves 2305 spectra with measured radial velocities.

We discovered during our reduction of the data that the 600 l mm$^{-1}$ grism was slightly misaligned in its IMACS holding cell during our observing run. As a result, there were

systematic errors in the model of the spectral traces in the detector plane. These errors caused some of the spectral traces to overlap on the detector, because the slitmask design program `intgui` had assumed the wrong model for spectral traces. The overlapping traces produce severe artifacts in the extracted spectra that lead to the above rejections. In total, we lost approximately 30% of our observed spectra to overlap-related artifacts.

## 2.5. Systematic Velocity Errors

In slit spectroscopy, there is the potential for systematic velocity errors introduced by misalignments of the star and slit. The magnitude of the error is $\Delta v = c \times \Delta\theta \times p/\lambda_0$, where $c$ is the speed of light, $\Delta\theta$ is the angular offset of the star from the slit center in arcseconds, $p$ is the spectral resolution in Å arcsec$^{-1}$ (2.9 for these data), and $\lambda_0$ is a characteristic wavelength for the measured features ($\sim 8600$ Å for the Ca II triplet).

Applying the above formula in a straightforward manner implies that the systematic velocity error due to pointing could be as high as 50 km s$^{-1}$, for a star positioned at the edge of the slit. However, in practice the real systematic error will never be this large, because it is mitigated by the finite size of the star's image. We define an "effective" pointing offset, $\Delta\theta_{eff}$, which is the offset from the slit center of the centroid of the star's flux distribution in the slit. Because the seeing was consistently of order the width of our slits (1″), the effective worst-case velocity uncertainty for a star centered at the edge of the slit is actually around 25 km s$^{-1}$. The iterative pointing procedure we employed (see Section 2.2) is designed to minimize such pointing errors, and results in a positioning of the field to within 0.2″. This is also equivalent to the internal astrometric precision of the MCPS catalog. Adopting 0.2″ as a characteristic pointing uncertainty yields a systematic velocity uncertainty due to pointing errors of 10 km s$^{-1}$.

In some of our fields, we detected a systematic radial-velocity gradient across the field, which we attribute to a small error in the rotational orientation of the slitmask. We were able to measure this error in the field orientation by examining the positions of the stars' spectral traces along the spatial dimension, because such a field-rotation error introduces a linear gradient in the spectral-trace positions in the Declination direction. Therefore, by measuring the gradient in the peak positions of the spectral trace as a function of Declination, we can constrain the field-rotation error. This is illustrated for one of the fields (Field 07) in Figure 6, in which we show the measured peak position of the spectra in the spatial direction as a function of both Right Ascension and Declination. As expected, there is no observed gradient in Right Ascension, and the gradient in Declination is well-matched by the predicted effect of a rotational error of $-0.45°$. We fit the measured peak positions in

each field in this manner to determine the best-fit field-rotation error for each field.

The field-rotation error also induces a complementary artificial radial-velocity gradient along the Right Ascension direction in each field. In Figure 7, we show the measured radial velocities of stars in Field 07 as a function of Right Ascension (open circles), and the corrected velocities predicted by our measurement of the field-rotation correction of $-0.45°$ (filled circles). In each field for which we determined a non-zero rotation error, applying a correction in this manner flattens the observed radial-velocity gradient, and in most cases reduces the RMS scatter of the velocity distribution by up to 16%. Applying this correction introduces an additional uncertainty due to uncertainty in the best-fit rotation angle. This uncertainty is indicated with the error bars in Figure 7. The magnitude of the uncertainty depends on the goodness-of-fit of the field-rotation correction, and also increases linearly with the offset of a given slit from the field center, in the Right Ascension direction.

During the analysis of Fields 01 and 06, we found evidence of large pointing errors involving both translation and rotation. The rotation errors in Field 06 were so large that stars near the top and bottom of the field lay outside the bounds of their slits. In both fields, the mean position of the spectral peaks in the spatial direction was several pixels away from the center of the slit. While we cannot directly measure the mean offset in the dispersion direction, the error in the spatial direction is cause for concern about the absolute velocity measurements in these fields. We choose to exclude the 226 stars in these fields from our analysis of the SMC kinematics. However, we note that the data from Fields 01 and 06 will be included in Paper II, since the metallicity analysis depends only on the equivalent widths of the Calcium lines, and not on their wavelengths.

The coordinates and velocities for the final sample of 2079 stars for which we measured velocities are presented in Table 2. The observed (topocentric) radial velocities are corrected to the heliocentric reference frame, using the IRAF task `rvcorrect`. The columns of Table 2 are: (1) an identification number for the object; (2) the Right Ascension coordinate; (3) the Declination coordinate; (4) the $V$ magniutde; (5) the $I$ magnitude; (6) the observed topocentric radial velocity; (7) the radial velocity, corrected to the Heliocentric frame; (8) the 1-$\sigma$ uncertainty in the positive $v_r$ direction; and (9) the 1-$\sigma$ uncertainty in the negative $v_r$ direction. The estimated radial-velocity uncertainties in columns 8 and 9 are usually dominated by the error due to the pointing precision of $0.2''$. They also include uncertainties associated with the field-rotation correction (see Figure 7), internal uncertainties from our measurement of the Ca II triplet lines, and the uncertainty of the wavelength calibration (see Figure 4). The remaining discussion employs the corrected heliocentric radial velocities.

In Table 1, we present additional data for the twelve fields which were observed. The additional columns are: (5) the number of RGB stars with a measured radial velocity; (6)

the mean radial velocity from a best-fit Gaussian; (7) the velocity dispersion from a best-fit Gaussian; (8) result of a K-S test investigating variations in the velocity distributions (see Section 3); (9) the best-fit field-rotation correction angle; and (10) the mean radial-velocity uncertainty due to the field-rotation correction.

## 2.6.   Comparison to Previous Measurements

When designing our target sample, we specifically set out to include red giant stars in the SMC whose radial velocities had been determined by previous authors. Unfortunately, very few such studies exist, and we found only one, Da Costa & Hatzidimitriou (1998), that reported observations of individual SMC giants. Of the seven SMC clusters targeted in that study, only Lindsay 11 falls within the bounds of the MCPS. We observed three of the six red giants in Lindsay 11 that were observed by Da Costa & Hatzidimitriou (MJD 182, MJD 212, and MJD 240, see Table 2). While Da Costa & Hatzidimitriou report the mean cluster velocity for Lindsay 11 ($132\pm5$ km s$^{-1}$), they do not report the individual velocities of the six giants they observed. The mean velocity of our three Lindsay 11 stars is $137\pm5$ km s$^{-1}$, in good agreement with the Da Costa & Hatzidimitriou (1998) result.

## 2.7.   Removing Foreground Contaminants

We expect our photometrically-selected sample to include a small number of foreground Milky Way main sequence dwarfs. Many of these contaminants can be identified by their radial velocity. However, some overlap in radial velocity is inevitable, so a second criterion is needed to cleanly remove the foreground population. We employ the Na doublet absorption feature at (8183 Å and 8195 Å), which is sensitive to surface gravity (*i.e.*, it is strong in dwarfs, and weak or absent in giants).

In Figure 8, we plot radial velocity against the equivalent width of the Na doublet for the subset of stars in our sample in which the Na doublet was measured. The foreground population is the set of points with low velocity and large EW(Na). However, there is a small population of objects that have large EW(Na), but also have large velocities. We visually inspected the objects for which EW(Na)$\gtrsim1$ and $v_r \gtrsim 50$ km s$^{-1}$, finding that some of the large measured EW(Na) values were spurious, or affected by obvious artifacts. The dotted line in Figure 8 indicates our adopted separation between dwarfs and giants. In addition to the 14 foreground stars shown in Figure 8, 14 more objects are flagged as foreground objects, solely on the basis of their SMC-discrepant radial velocities ($v_r < 50$ km s$^{-1}$ or

$v_r > 250$ km s$^{-1}$). EW(Na) could not be measured properly in these objects, usually due to extraction artifacts or the gap between CCDs in the detector array. The 33 stars determined to be unassociated with the SMC are flagged in Table 2, and are omitted from the remaining discussion.

## 3. SMC Kinematics and Dynamical Structure

In Figure 9, we show the global distribution of radial velocities of the 2046 SMC stars in our sample. It is evidently well-fit by a Gaussian, which has a mean velocity of $145.6 \pm 0.6$ km s$^{-1}$ and a velocity dispersion of $27.6 \pm 0.5$ km s$^{-1}$. This compares well with previous radial-velocity studies of the SMC, as shown in Table 3. It is interesting to note that all kinematic studies of the SMC show rough agreement in their mean heliocentric radial velocity ($\sim 150$ km s$^{-1}$) and velocity dispersion ($\sim 25$ km s$^{-1}$), regardless of the age of the objects sampled, from HI gas shells to red giant stars.

A more detailed inspection of our velocity distribution reveals that the mean velocity of stars in each field varies significantly, from 129 to 156 km s$^{-1}$ (see Table 1). K-S tests indicate that while most of the fields are consistent with having been drawn from the same parent distribution, there are some statistically significant (probability of random $< 10^{-3}$) exceptions: fields 02, 05, 08 and 13. To investigate whether these field-to-field variations represent a global kinematic trend, such as systemic rotation or viewing angle dependent effects, we fit a plane to the velocity distribution on the sky. Fitting a plane is a simple first order model, and can represents either solid body rotation or velocity gradients caused by the projection of differing amounts of the Galactocentric tangential SMC velocity onto the line-of-sight toward one side or the other of the SMC. A fit to all of the stars in the sample results in an excellent fit ($\chi^2 = 1.15$) with an apparent rotation amplitude of 8.3 km s$^{-1}$ deg$^{-1}$ and a rms scatter of $27.5 \pm 0.5$ km s$^{-1}$. The apparent kinematic major axis, that of the largest velocity gradient, is at $23.4°$ East of North. The skewness of the velocity distribution is -0.11 and the excess kurtosis (above that for a Gaussian) is 0.09. The quality of the fit, as quantified by the low $\chi^2$ value, and the low amplitude of higher order moments demonstrates that with these data there is no justification to proceed to more complex fitting models.

The interpretation of the observed velocity gradient is complicated by the large angular extent of the galaxy on the sky. Because of the SMC's large size, the tangential velocity of the SMC is projected with different sign on the two sides of the galaxy, thereby creating an apparent rotation signature (while the radial velocity is projected with the same sign). Correcting for this effect requires a high-precision measurement of the SMC's proper motion. The most recent measurement of the SMC's proper motion still has uncertainties that are $>50\%$ (Kroupa & Bastian 1997). A more precise measurement, with an uncertainty $\sim 5\%$, has recently been presented for the LMC (Kallivayalil et al. 2005). The latter translates to a tangential velocity of 493 km s$^{-1}$ for the LMC (the earlier SMC measurement also suggested a tangential velocity of $\sim 500$ km s$^{-1}$). If we adopt

a tangential velocity of 500 km s$^{-1}$ for the SMC, and allow its direction to be a free parameter, then we can place limits on the effect this motion has on the magnitude of our measurement of a rotation velocity by assuming the full effect of the projected tangential motion is either parallel or antiparallel to that observed. The adopted tangential velocity will result in an apparent velocity gradient of 8.7 km s$^{-1}$ deg$^{-1}$ over the face of the SMC. This value suggests that the entire velocity gradient observed could be accounted for by this effect, so it is possible that there is no intrinsic rotation in the SMC at all. If the result of the projected tangential motion is oriented in the opposite direction, then the true velocity gradient due to rotation could be as much as 17 km s$^{-1}$ deg$^{-1}$. In the direction for which the gradient is measured, the regions of the SMC that was observed extends about 1° and hence the maximum rotation velocity over the observed region would be about 17 km s$^{-1}$. Even adopting this largest correction, the rotation velocity is still significantly less than the velocity dispersion: $v/\sigma \leq 0.6$, so we can conclude that the SMC is primarily supported by its velocity dispersion.

## 3.1. Morphology and Dynamics

The connection between the shapes of spheroids and their internal kinematics has been investigated for both giant and dwarf ellipticals (see Davies et al. 1983; de Zeeuw & Franx 1991). Low luminosity systems generally agree with the expectations drawn from models of oblate rotators: their degree of flattening is consistent with the expectation of rotational support and an isotropic velocity dispersion tensor. We test whether the SMC exhibits the same behavior.

We use the stellar catalog presented in Zaritsky et al. (2002), and their same photometric cuts ($16 \leq V \leq 19.5$, $B - V > 0.7$) to isolate the older stellar population in the SMC. A stellar density image of the SMC corresponding to this population is created by doing a gnomic projection of the coordinates, and accumulating the flux of these stars in 100″ "pixels". This image is then analyzed using the IRAF ellipse fitting routines and the results are plotted in Figure 10. The top two panels show the positional offset of the center of each elliptical isophote, relative to the innermost ellipse (with a radius of 30′), in units of 100″. The third panel shows the ellipticity ($e = 1 - b/a$) of each ellipse, and the fourth shows the position angle of each ellipse's major axis (measured to the East from North).

The profiles shown in Figure 10 have several features that bear discussion. First, we have excluded the inner region ($r < 30′$) because of crowding-induced incompleteness in the photometric catalog. Second, beyond that radius the position angle of isophotes varies by about 20°, possibly indicating a triaxial stellar distribution that is not viewed along any of the principal axes. However, it is possible that the incompleteness effects extend beyond 30′, and these effects could potentially cause the observed isophotal twisting. Third, at radii beyond 70′, the position of the centroid, the ellipticity, and the isophotal position angle remain constant. The constant position angle suggests that at these radii we are viewing the stellar distribution nearly along a principal axis,

and that therefore the ellipticity reflects the true axis ratio. For radii $> 70'$, the mean values of the ellipticity and position angle (measured from North to East) are 0.30 and 49°, respectively. These values are in rough agreement with measurements by de Vaucouleurs (1955), who found $e = 0.58$ and $PA = 45° \pm 2°$.

In Figure 11 we show how the ellipticity and $v/\sigma$ compare to other spheroids. We have taken the data from Davies et al. (1983) for comparison and plotted the relationship for an oblate rotator with an isotropic velocity dispersion tensor. The shaded area represents where the SMC lies depending on the nature of the correction due to the unknown transverse velocity. The shape and internal kinematics of the SMC are in the range observed for dwarf ellipticals. Its position in this diagram demonstrates that its shape is consistent with rotational flattening.

Using the morphological parameters, we define elliptical annuli in which we evaluate the velocity dispersion (Figure 12). The velocity dispersion is roughly flat as a function of radius, with perhaps a slight rise with increasing radius. Once again we find no signature of disturbance or deviations from the expectations for a relaxed spheroidal system.

## 3.2. Mass

Using a highly simplified application of the tensor virial theorem (assuming a steady-state SMC, an isotropic velocity dispersion, no projection correction to the rotational velocity, and the potential energy of a uniform sphere),

$$v^2 + \sigma^2 = \frac{3GM}{5R},$$

we estimate the mass of the SMC out to our last measured point, 1.6 kpc. For a line-of-sight velocity dispersion of 27.5 km s$^{-1}$, which for the assumption of isotropy implies a true velocity dispersion of 48 km s$^{-1}$, and a rotation velocity that is somewhere between 0 and 17 km s$^{-1}$, we derive that the enclosed mass is between $1.4 \times 10^9 M_\odot$ and $1.9 \times 10^9 M_\odot$. In order to compare to the mass measurement obtained by Stanimirović et al. (2004) from the HI rotation curve, we can extend the analysis to 3 kpc by assuming that the velocity dispersion remains constant, and that the velocity gradient can be extrapolated. In this case, we derive an enclosed mass between $2.7 \times 10^9 M_\odot$ and $5.1 \times 10^9 M_\odot$. This range of values is slightly larger than the mass determined from the HI rotation curve over the same radius ($2.4 \times 10^9 M_\odot$; Stanimirović et al. 2004), but consistent given the uncertainties and gross simplifications in our analysis. A precise value for the proper motion for the SMC will warrant a more complete dynamical treatment and is also necessary to examine higher order moments of the velocity field.

## 4.   Summary

We present the first spectroscopic survey of field red giant stars over the main body of the Small Magellanic Cloud. Our spectroscopic sample includes over 3000 red giants in 14 28' fields spanning the central $2° \times 1°$ of the SMC. After rejecting two fields due to unresolved pointing errors and losing additional spectra to overlap issues, our final kinematic sample contains 2079 stars throughout the central 3.9 kpc×1.8 kpc, of which 2046 are determined to be SMC members. The global velocity distribution is well-fit by a Gaussian centered at 146 km s$^{-1}$ with a width or $\sigma$ of 28 km s$^{-1}$, but we also find evidence for a velocity gradient across the SMC. Removing the gradient using a planar fit to the velocities results in an rms scatter ($27.5 \pm 0.5$ km s$^{-1}$) that is effectively unchanged from the global velocity dispersion measured prior to any correction because the amplitude of the fitted rotation gradient (7.9 km s$^{-1}$ deg$^{-1}$) is small. The origin of the velocity gradient could be either internal rotation or an illusion caused by the differential projection of the SMC's tangential velocity along non-parallel lines of sight. Without a high precision measurement of the SMC's proper motion, a sufficiently precise correction required to recover the SMC's intrinsic rotation speed is impossible. However, even adopting the maximum correction we find that $v < \sigma$ and hence that the SMC is primarily supported by its velocity dispersion.

We find that the shape of the SMC, as measured from the analysis of the spatial distribution of red giant stars, is consistent with the degree of rotational flattening expected for the observed $v/\sigma$ (Figure 11). As such, the properties of the SMC are consistent with similar low luminosity spheroidal systems. We conclude that the SMC is a low luminosity spheroid whose visual appearance is dominated by star formation resulting from a recent accretion of gas (see also Zaritsky et al. 2000). The underlying morphology and dynamics are consistent with those of low luminosity ellipticals.

A simple virial analysis using the measured kinematics implies an enclosed mass within 1.6 kpc of between 1.4 and $1.9 \times 10^9 M_\odot$, and a less well constrained mass of between 2.7 and $5.1 \times 10^9 M_\odot$ within 3 kpc. These values are larger than those inferred from the HI kinematics ($2.4 \times 10^9 M_\odot$, Stanimirović et al. 2004), but the simplifying assumptions used could easily account for differences at the factor of two level.

## REFERENCES

Bigelow, B. C., Dressler, A. M., Shectman, S. A., & Epps, H. W. 1998, in Proc. SPIE Vol. 3355, p. 225-231, Optical Astronomical Instrumentation, Sandro D'Odorico; Ed., 225–231

Crowl, H. H., Sarajedini, A., Piatti, A. E., Geisler, D., Bica, E., Clariá, J. J., & Santos, J. F. C. 2001, AJ, 122, 220

Da Costa, G. S. & Hatzidimitriou, D. 1998, AJ, 115, 1934

Davies, R. L., Efstathiou, G., Fall, S. M., Illingworth, G., & Schechter, P. L. 1983, ApJ, 266, 41

de Vaucouleurs, G. 1955, AJ, 60, 219

de Zeeuw, T. & Franx, M. 1991, Ann. Rev. Astron. & Astroph., 29, 239

Dopita, M. A., Lawrence, C. J., Ford, H. C., & Webster, B. L. 1985, ApJ, 296, 390

Gardiner, L. T. & Hawkins, M. R. S. 1991, MNRAS, 251, 174

Gardiner, L. T. & Noguchi, M. 1996, MNRAS, 278, 191

Groenewegen, M. A. T. 2000, A&A, 363, 901

Hardy, E., Suntzeff, N. B., & Azzopardi, M. 1989, ApJ, 344, 210

Harris, J. 2005, *in preparation*

Harris, J. & Zaritsky, D. 2004, AJ, 127, 1531

Hatzidimitriou, D., Cannon, R. D., & Hawkins, M. R. S. 1993, MNRAS, 261, 873

Hatzidimitriou, D., Croke, B. F., Morgan, D. H., & Cannon, R. D. 1997, A&AS, 122, 507

Hatzidimitriou, D. & Hawkins, M. R. S. 1989, MNRAS, 241, 667

Kallivayalil, N., van der Marel, R. P., Alcock, C., Axelrod, T., Cook, K. H., Drake, A. J., & Geha, M. 2005, ApJ(submitted), astro-ph/050845

Kroupa, P. & Bastian, U. 1997, New Astronomy, 2, 412

Lah, P., Kiss, L. L., & Bedding, T. R. 2005, MNRAS, 359, L42

Mathewson, D. S., Cleary, M. N., & Murray, J. D. 1974, ApJ, 190, 291

Mathewson, D. S., Ford, V. L., & Visvanathan, N. 1986, ApJ, 301, 664

—. 1988, ApJ, 333, 617

Maurice, E., Andersen, J., Ardeberg, A., Bardin, C., Imbert, M., Lindgren, H., Martin, M., Mayor, M., Nordstrom, B., Prevot, L., Rebeirot, E., & Rousseau, J. 1987, A&AS, 67, 423

Stanimirović, S., Staveley-Smith, L., & Jones, P. A. 2004, ApJ, 604, 176

Staveley-Smith, L., Sault, R. J., Hatzidimitriou, D., Kesteven, M. J., & McConnell, D. 1997, MNRAS, 289, 225

Suntzeff, N. B., Friel, E., Klemola, A., Kraft, R. P., & Graham, J. A. 1986, AJ, 91, 275

Welch, D. L., McLaren, R. A., Madore, B. F., & McAlary, C. W. 1987, ApJ, 321, 162

Zaritsky, D. & Harris, J. 2004, ApJ, 604, 141

Zaritsky, D., Harris, J., Grebel, E. K., & Thompson, I. B. 2000, ApJ, 534, L53

Zaritsky, D., Harris, J., Thompson, I. B., Grebel, E. K., & Massey, P. 2002, AJ, 123, 855

Table 1.   Targeted IMACS Fields

| ID | R.A. [h : m : s] | Dec. [d : m] | $N_{slits}$ | $N_{RGB}$ | $< v_{rad} >$ [km s$^{-1}$] | $\sigma$ [km s$^{-1}$] | KS prob. | $\theta_{err}$ [°] | $< \sigma_{v,\theta} >$ [km s$^{-1}$] |
|---|---|---|---|---|---|---|---|---|---|
| 01[a] | 0:03:12 | −72:12 | 255 | · · · | · · · | · · · | · · · | · · · | · · · |
| 02 | 0:03:48 | −72:12 | 293 | 190 | 129±2 | 28±2 | $2 \times 10^{-8}$ | 0.00 | 1.0 |
| 03 | 0:04:24 | −72:12 | 256 | 160 | 147±3 | 26±4 | 0.88 | 0.00 | 2.5 |
| 04 | 0:05:00 | −72:12 | 146 | 115 | 151±3 | 20±2 | 0.06 | 0.00 | 1.4 |
| 05 | 0:03:12 | −72:42 | 341 | 223 | 136±2 | 27±2 | $7 \times 10^{-4}$ | −0.10 | 7.6 |
| 06[a] | 0:03:48 | −72:42 | 351 | · · · | · · · | · · · | · · · | · · · | · · · |
| 07 | 0:04:24 | −72:42 | 282 | 189 | 151±2 | 21±2 | 0.03 | −0.45 | 7.0 |
| 08 | 0:05:00 | −72:42 | 159 | 123 | 156±2 | 23±2 | $5 \times 10^{-4}$ | −0.15 | 4.6 |
| 09[b] | 0:02:55 | −73:05 | 359 | · · · | · · · | · · · | · · · | · · · | · · · |
| 10[b] | 0:03:31 | −73:05 | 346 | · · · | · · · | · · · | · · · | · · · | · · · |
| 11 | 0:04:07 | −73:06 | 304 | 193 | 148±2 | 25±2 | 0.60 | −0.12 | 8.6 |
| 12 | 0:02:38 | −73:30 | 326 | 218 | 146±2 | 28±2 | 0.90 | −0.30 | 6.1 |
| 13 | 0:03:14 | −73:30 | 341 | 200 | 154±2 | 25±2 | $1 \times 10^{-3}$ | −0.25 | 3.8 |
| 14 | 0:03:50 | −73:30 | 300 | 205 | 149±2 | 27±2 | 0.72 | −0.25 | 5.5 |
| 15 | 0:02:00 | −73:12 | 174 | 131 | 141±3 | 21±3 | 0.10 | −0.35 | 4.4 |
| 16 | 0:02:00 | −72:42 | 122 | 99 | 148±3 | 20±4 | 0.83 | −0.50 | 2.2 |

[a]Field discarded due to pointing errors

[b]Field not observed

Table 2.   Red Giant Stars in the SMC

| ID | R.A. (h : m : s) | Dec. (d : m : s) | V (mag) | I (mag) | $v_{r,obs}$ (km s$^{-1}$) | $v_{r,corr}$ (km s$^{-1}$) | $+\sigma$ (km s$^{-1}$) | $-\sigma$ (km s$^{-1}$) |
|---|---|---|---|---|---|---|---|---|
| s02_0011 | 00:55:39.6 | −72:15:59 | 17.24 | 16.11 | 134.1 | 128.7 | 3.2 | 3 .0 |
| s02_0015 | 00:54:06.1 | −72:07:31 | 17.07 | 15.85 | 113.7 | 108.3 | 3.5 | 3 .1 |
| s02_0018 | 00:54:46.4 | −72:06:08 | 17.29 | 16.14 | 157.0 | 151.7 | 4.3 | 4 .1 |
| s02_0023 | 00:55:22.6 | −72:07:05 | 17.18 | 16.03 | 120.0 | 114.7 | 6.1 | 5 .9 |
| s02_0031 | 00:57:04.5 | −72:15:26 | 17.07 | 15.89 | 157.5 | 152.2 | 2.5 | 2 .3 |
| s02_0035 | 00:57:38.7 | −72:20:18 | 16.89 | 15.62 | 112.3 | 107.0 | 3.1 | 2 .9 |
| s02_0039 | 00:58:58.3 | −72:20:39 | 17.34 | 16.20 | 129.7 | 124.4 | 2.9 | 2 .6 |
| s02_0040 | 00:59:12.5 | −72:17:59 | 17.01 | 15.82 | 97.7 | 92.4 | 2.6 | 2 .3 |
| s02_0046 | 00:58:20.7 | −72:11:24 | 17.12 | 15.94 | 105.3 | 100.0 | 2.5 | 2 .4 |
| s02_0048 | 00:59:02.6 | −72:07:16 | 17.23 | 16.07 | 164.3 | 159.1 | 3.7 | 3 .5 |

[a]Member of Lindsay 11 observed by Da Costa & Hatzidimitriou (1998)

[b]Foreground star

Table 3.   SMC Radial Velocity Studies

| Reference | $v_{r,helio}$ [km s$^{-1}$] | $\sigma$ [km s$^{-1}$] | sample description |
|---|---|---|---|
| Dopita et al. (1985) | $146 \pm 4$ | $25 \pm 3$ | 44 planetary nebulae |
| Suntzeff et al. (1986) | 123 | 24.2 | 12 red giant stars near NGC 121 |
| Maurice et al. (1987) | $162 \pm 1$ | 18 | 255 supergiants and main sequence stars |
| Mathewson et al. (1988) | $149 \pm 3$ | $22 \pm 3$ | 61 cepheid stars |
| Hardy et al. (1989) | $148 \pm 4$ | $27 \pm 2$ | 131 central carbon stars |
| Hatzidimitriou et al. (1993) | $151 \pm 6$ | $33 \pm 4$ | 29 red clump stars in outer NE quadrant |
| Staveley-Smith et al. (1997) | $155 \pm 1$ | $25 \pm 1$ | 501 expanding HI shells |
| Hatzidimitriou et al. (1997) | $149 \pm 3$ | $26 \pm 2$ | 72 outer carbon stars |
| this work | $145.6 \pm 0.6$ | $27.6 \pm 0.5$ | 2046 red giant stars |
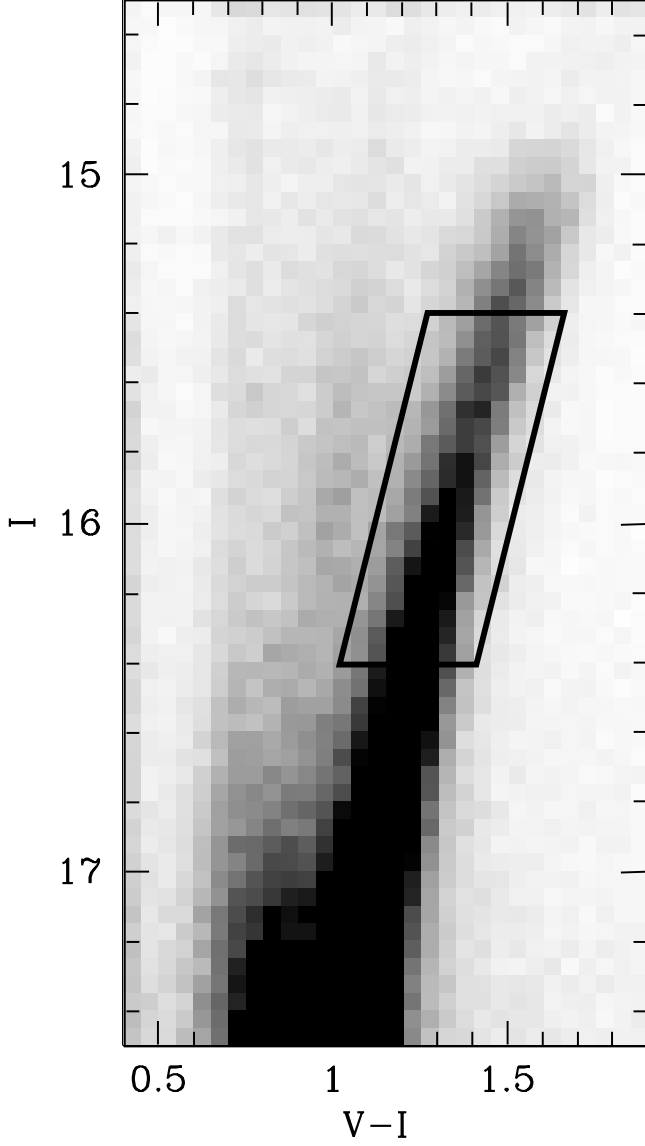
Fig. 1.— A V-I, I Hess diagram showing MCPS photometry of the red giant branch in the Small Magellanic Cloud. The black box illustrates the photometric criteria used to select 30,000 bright red giant candidates for our spectroscopic sample. The criteria were chosen to include the full range of RGB colors, and to avoid the tip of the RGB, where deep mixing may alter surface abundances.
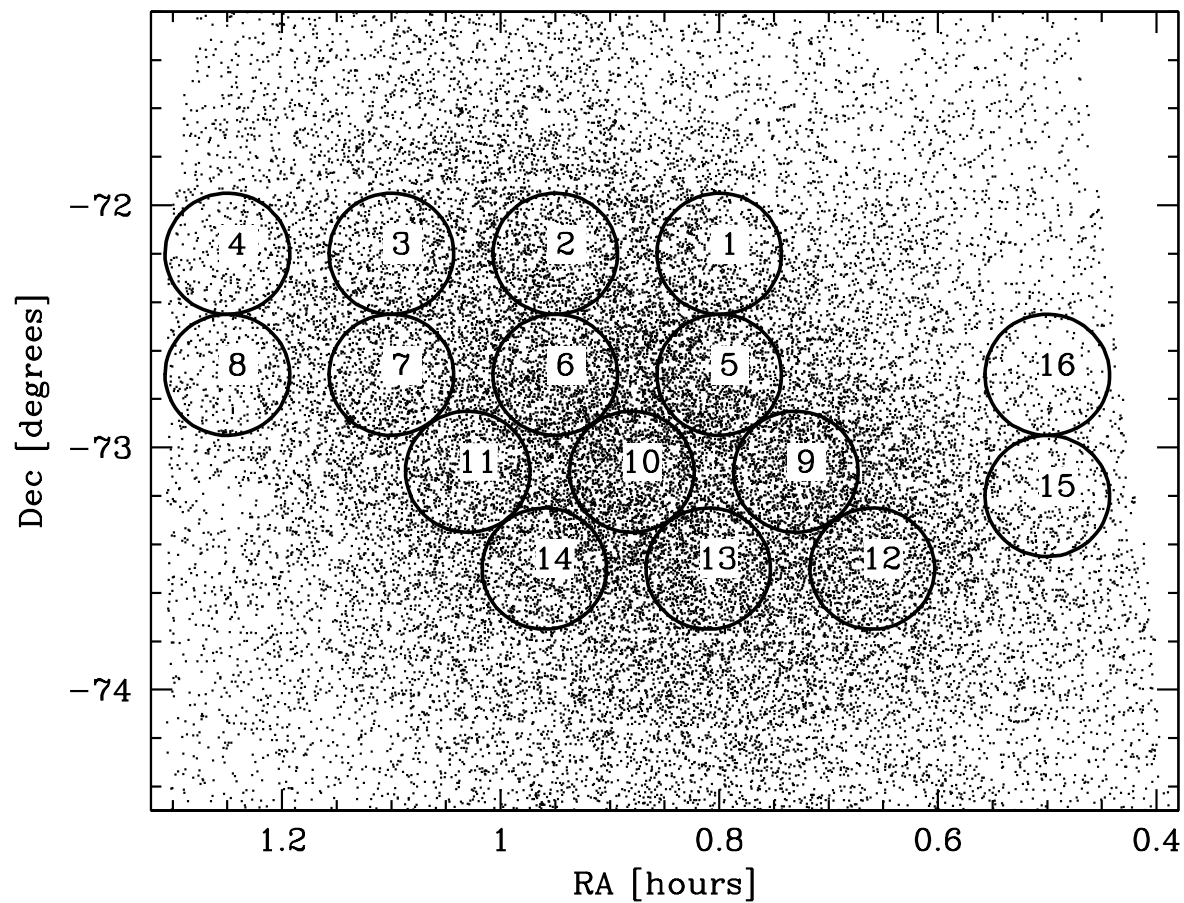
Fig. 2.— The distribution on the sky of the sixteen IMACS fields which were prepared for observation. The points show the distribution of 34,000 RGB candidates in the SMC, selected with the photometric criteria described in Section 2.1. Fields 9 and 10 were not observed.
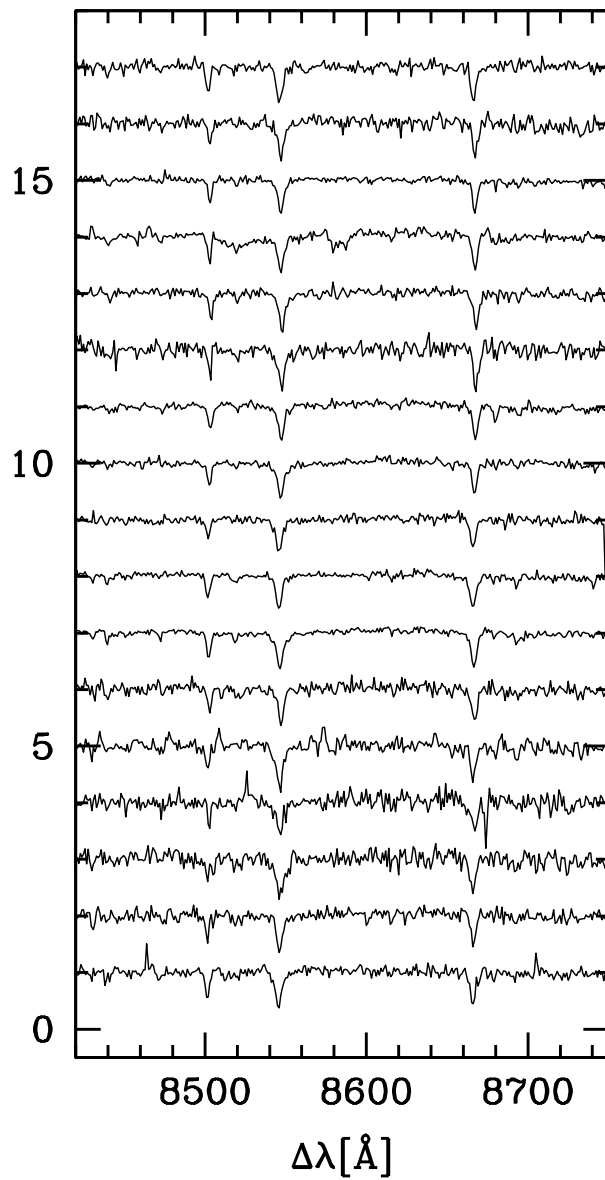
Fig. 3.— A sampling of extracted spectra from one of our fields (field 07), focusing on the Ca II triplet region.
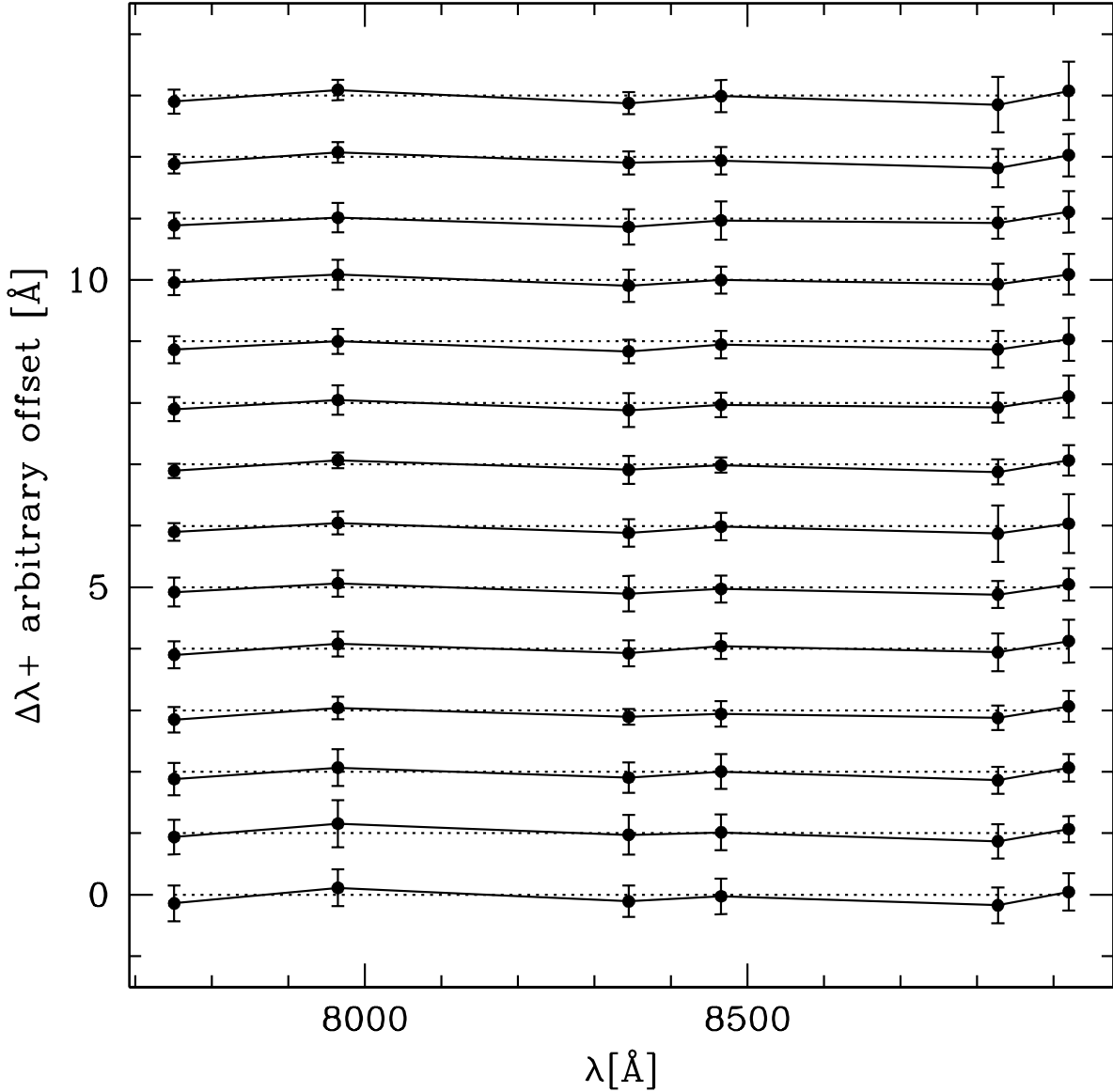
Fig. 4.— Checking for systematic errors in the wavelength calibration. We plot the deviation of the average measured wavelength for six bright sky emission lines in 2079 rectified, one-dimensional extracted spectra. Each set of connected points shows the results for one of our 14 observed fields, and the error bars indicate the standard deviation of the measurements of each line. The data for each field are given an arbitrary offset for clarity, and the dotted lines indicate the zero-deviation line for each field. While there are detectable systematic trends that are persistent across all fields, these deviations are within one standard deviation of the tabulated wavelength and smaller than the quoted random errors for individual stars.
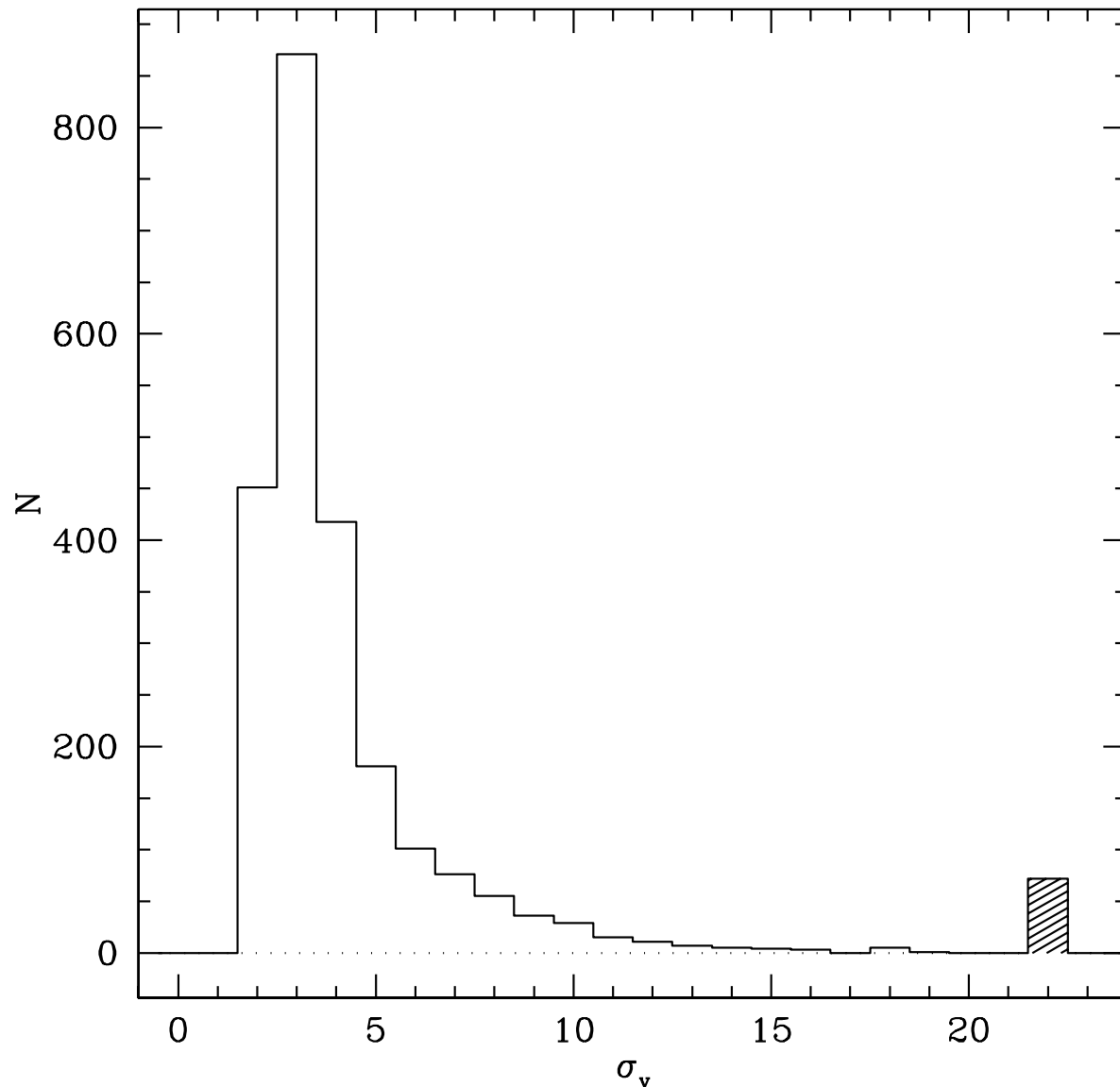
Fig. 5.— The distribution of measured radial velocity uncertainties, as derived from the Doppler shift of each spectrum (not including uncertainties from the Heliocentric correction or field-rotation errors). The distribution has a narrow peak at 3 km s$^{-1}$, and 97% of the stars have $\sigma_v < 20$ km s$^{-1}$. The shaded bin at the right indicates the number of stars with $\sigma_v > 20$ km s$^{-1}$. These stars are actually distributed more-or-less uniformly between 20 and 120 km s$^{-1}$, and are compressed into a single bin in the plot for clarity.
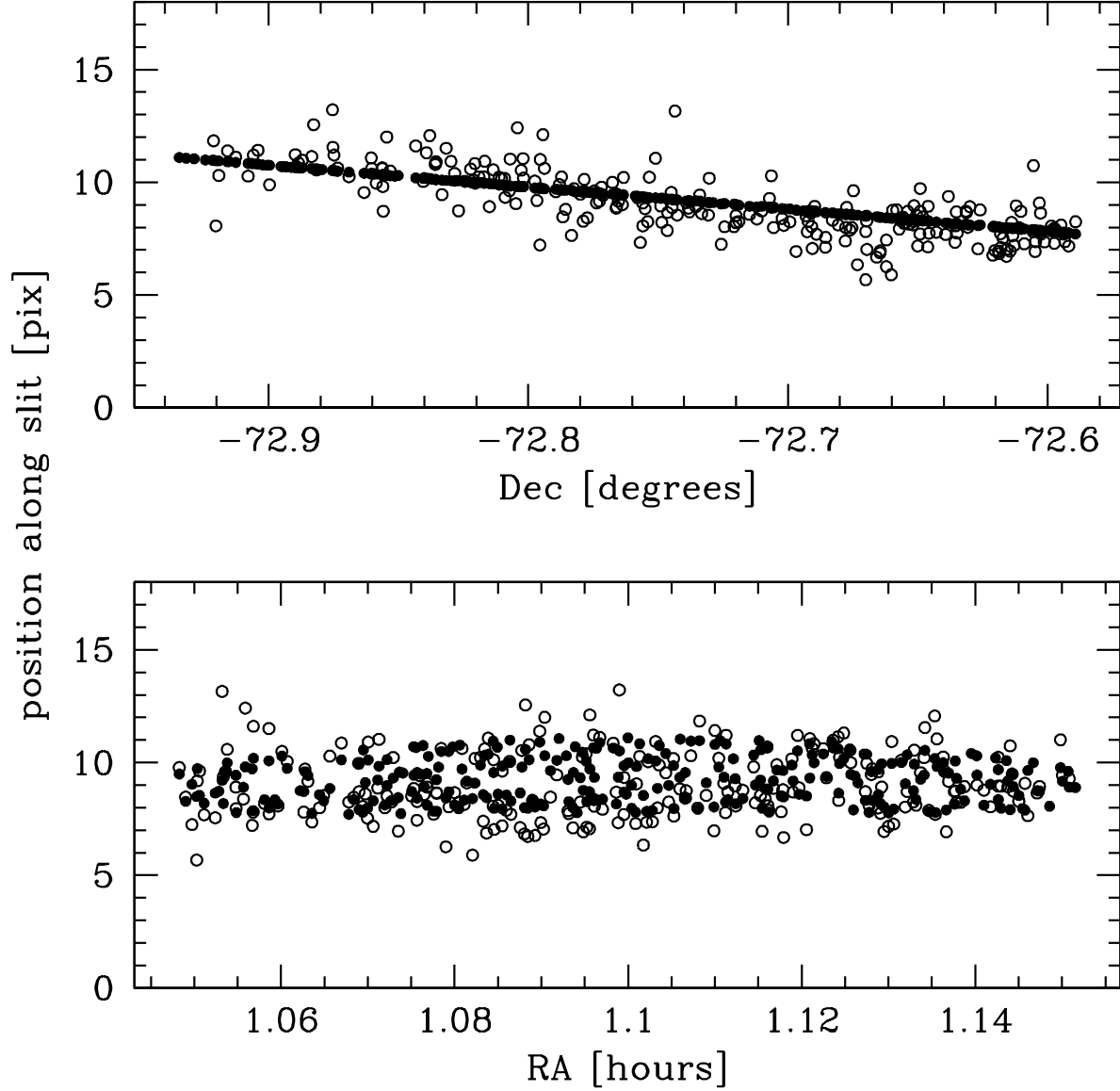
Fig. 6.— Open points: the measured position of the peak of the spectral trace along the spatial dimension, for the slits in field 07, vs. the slit's Right Ascension (bottom panel) and Declination (top panel). Filled points: the expected spectral-trace positions if there was a field-rotation error of -0.45°. We construct this plot for each field to constrain the field-rotation error, which we use to apply systematic velocity corrections.
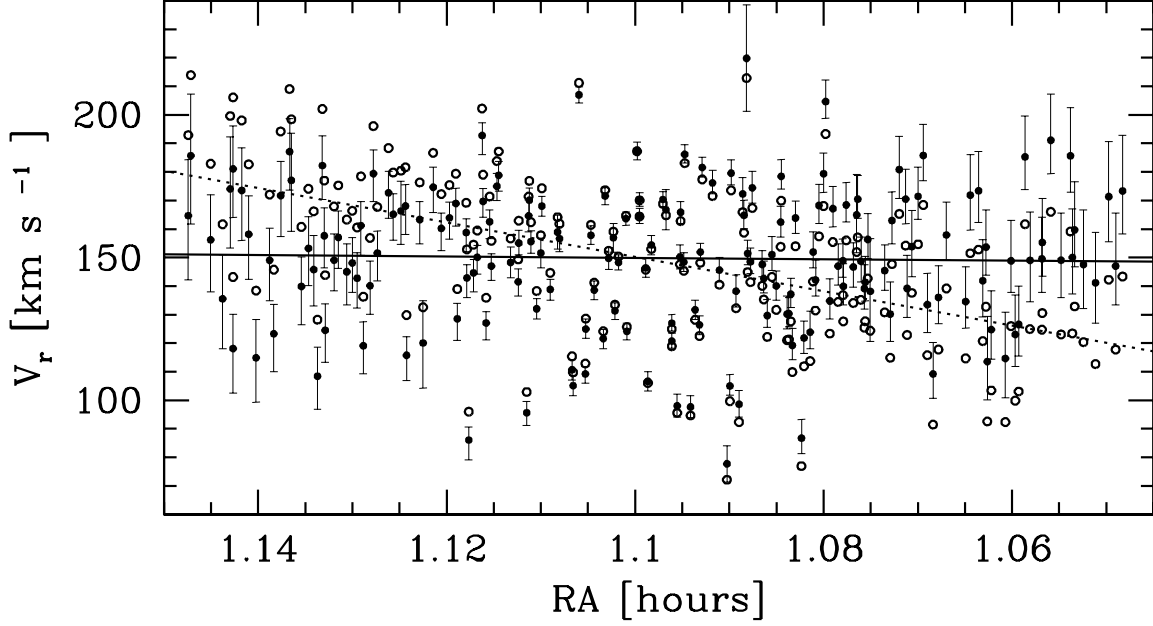
Fig. 7.— Open points: the measured radial velocities in field 07 as a function of Right Ascension. Solid points with errorbars: the radial velocities, after correcting for the field-rotation error as measured by the positions of the spectral traces. The dotted and solid lines are the best linear fits through the observed and corrected data, respectively. These fits reveal that the observed apparent velocity gradient was in fact an artifact due to the field-rotation error. This is found to be the case for each field for which a non-zero field-rotation error was measured.
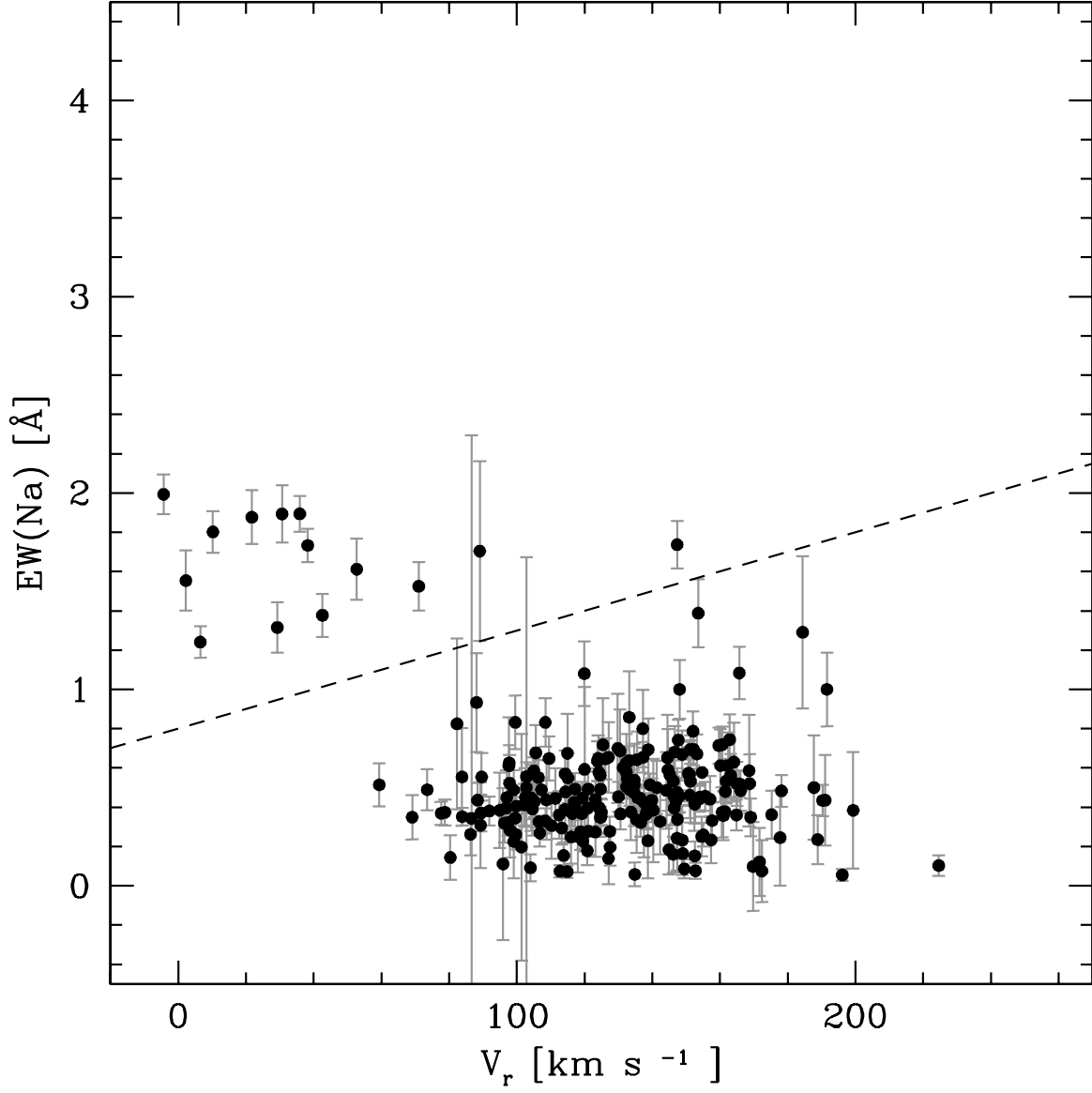
Fig. 8.— The total equivalent width of the Na doublet vs. the radial velocity of the star, for the subset of stars in which the Na doublet was detected. Foreground dwarfs in our sample will have low velocities and large EW(Na). Objects above the dashed line are identified as foreground stars in our sample.

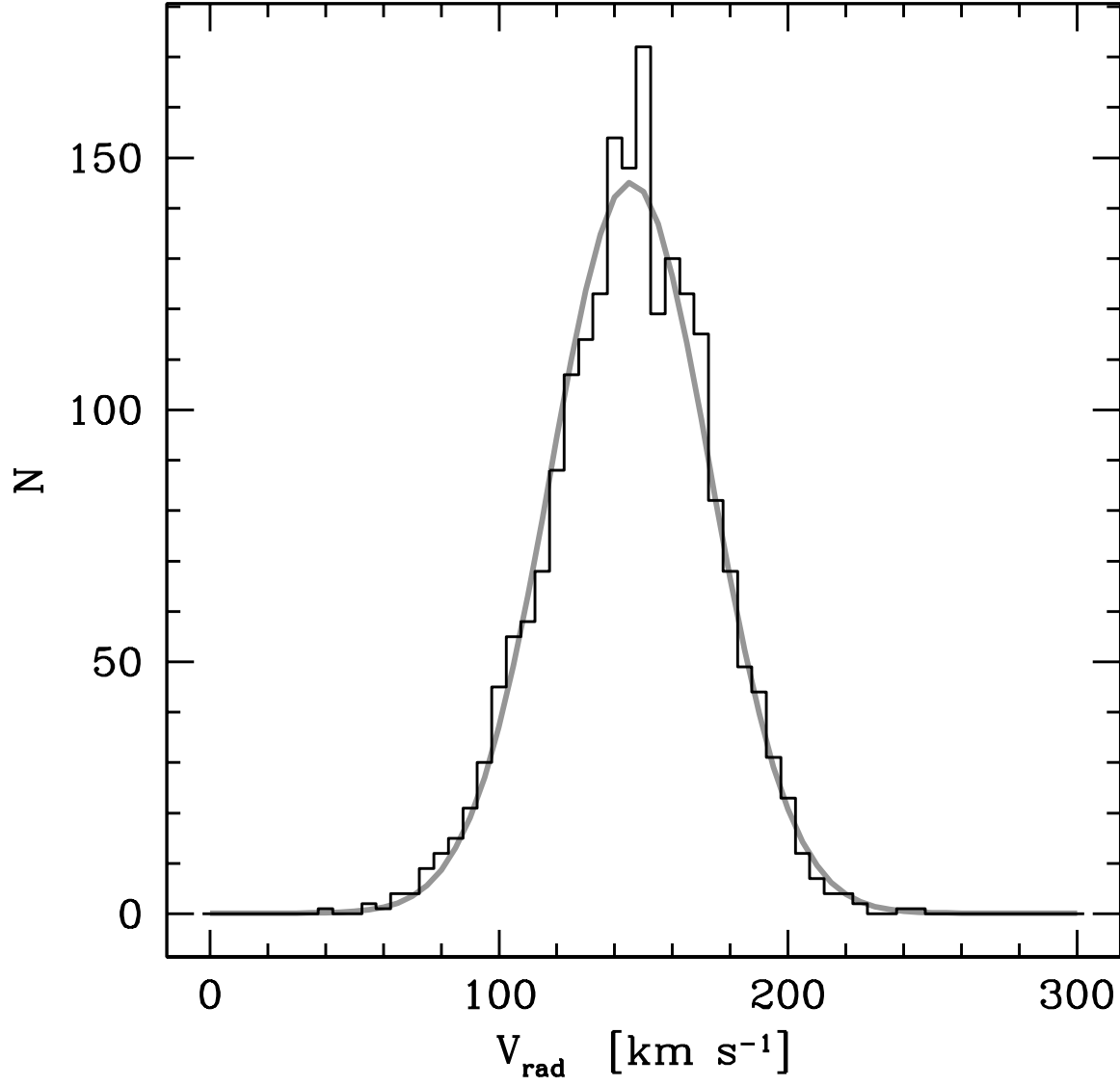Fig. 9.— Histogram: the distribution of radial velocities of 2046 red giants in the SMC. It is well-fit by a Gaussian (grey curve) centered at 146 km s$^{-1}$, with a dispersion of 28 km s$^{-1}$.
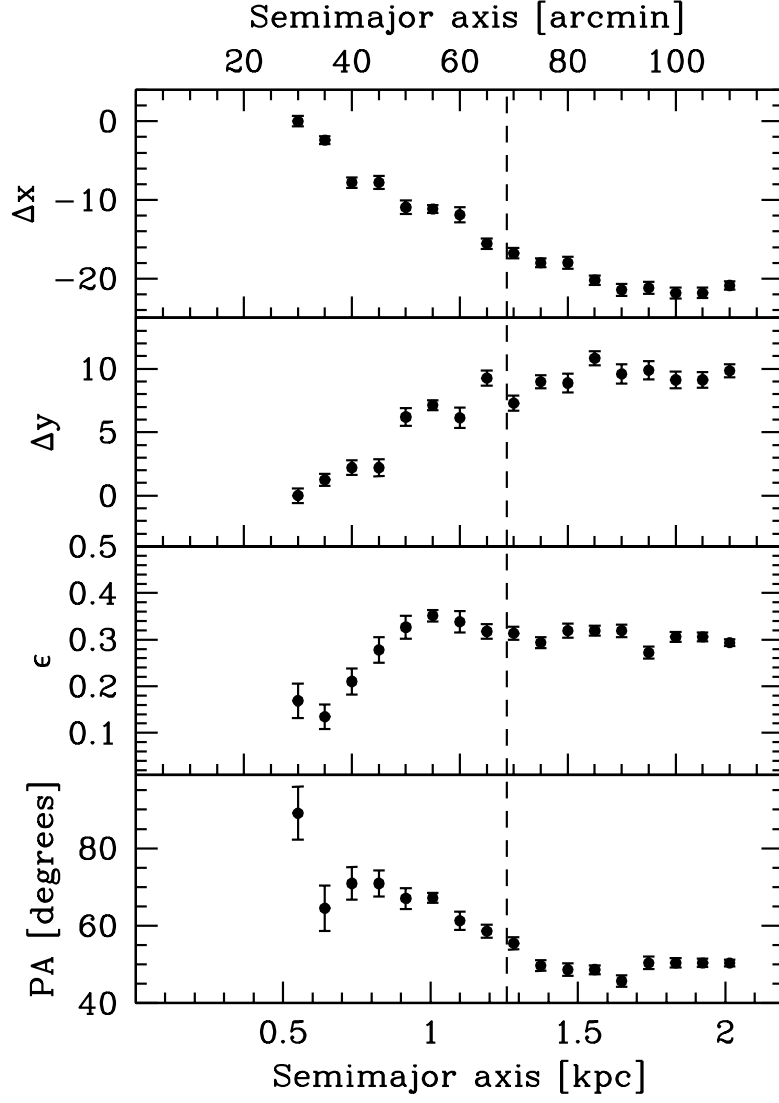
Fig. 10.— Isophote centroid position offset, ellipticity ($\epsilon$), and position angle radial profiles. Centroid offsets are in units of $100''$.

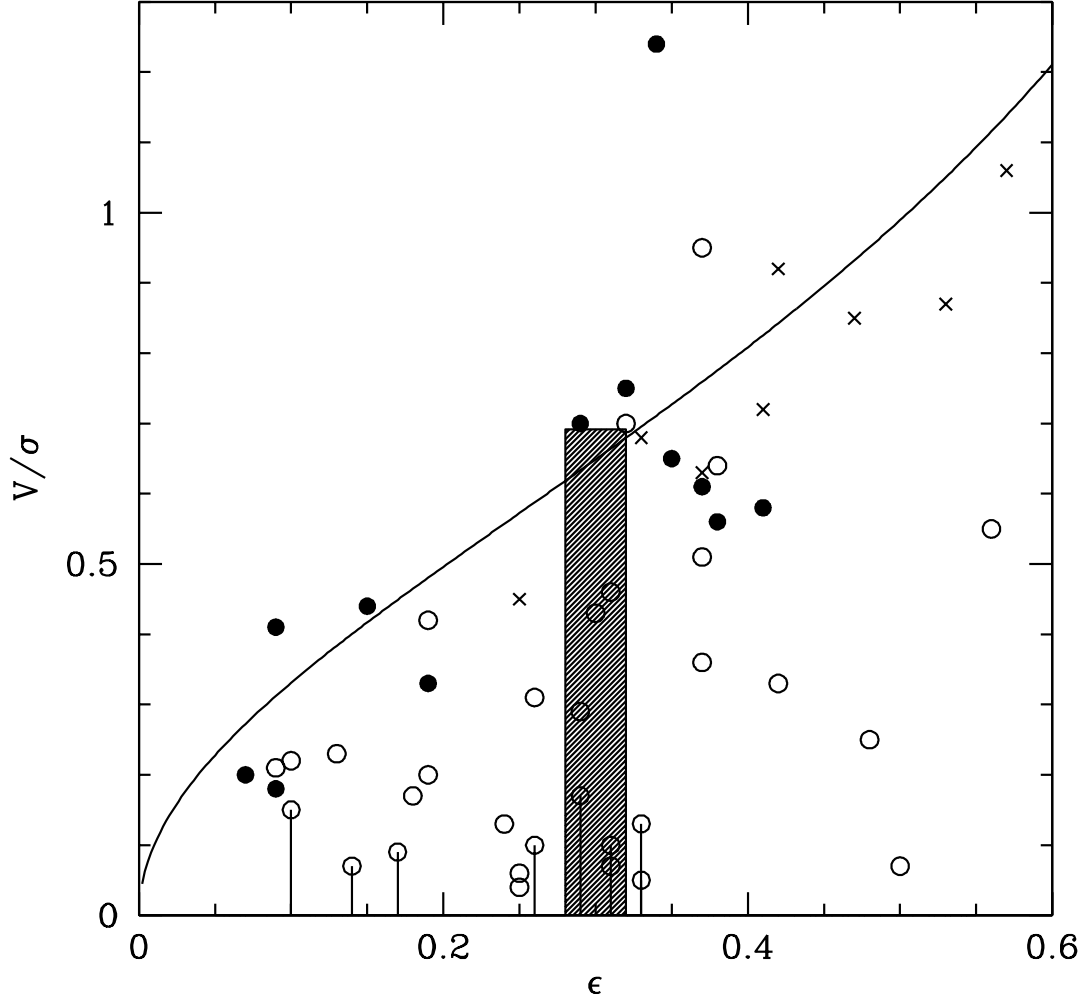Fig. 11.— The effect of rotation support. We show the distribution of ellipticity $(1 - b/a)$ vs. the ratio of rotational velocity to velocity dispersion. We plot the original data from Davies et al. (1983): low-luminosity $(M_B > -20.5$ mag) elliptical galaxies are shown with filled circles, and bright $(M_B < -20.5$ mag) elliptical galaxies are shown with open circles. Bulges of disk galaxies are shown with crosses. The expected relation for oblate isotropic rotators is shown with a solid curve. The range of values we derive as appropriate for the SMC is indicated by the shaded box.
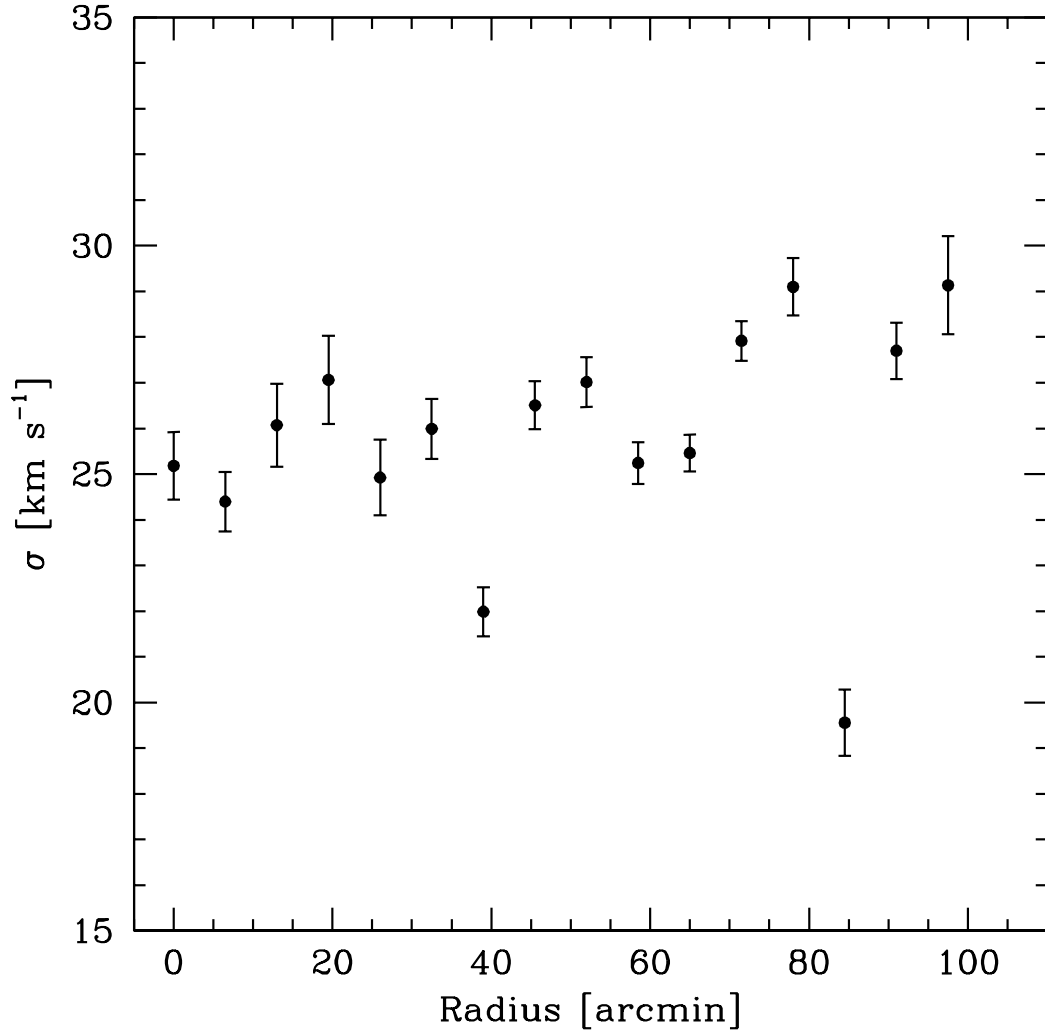
Fig. 12.— Velocity dispersion vs semimajor axis. The velocity dispersions are calculated using all stars within the elliptical annulus. The velocities used have been corrected for the linear velocity gradient.